npj | 2D Materials and Applications

www.nature.com/npj2dmaterials

ARTICLE OPEN

Check for updates

Synthesis of high-quality monolayer tungsten disulfide with chlorophylls and its application for enhancing bone regeneration

Yi-Wen Chen[1,2], Ming-You Shie[3,4], Chien-Hsuan Hsiao[5], Yu-Chun Liang[5], Ben Wang[6,7,8] and I-Wen Peter Chen[5]✉

Due to the population explosion of the 21st century, nearly one billion people are over 64 years of age and bone fracture is one of the most frequent problems facing both sexes because of osteoporosis. However, difficulty in enhancing bone regeneration to repair bone fracture poses challenges and thus, a two-dimensional monolayer material (i.e. tungsten disulfide (WS_2)) could be one of the candidates offering a possible solution to the problem. Here, we prepare high-quality monolayer WS_2 thin sheets in a large quantity with the assistance of extracted chlorophyll molecules, the natural pigment used in photosynthesis, via a liquid-phase exfoliation method. Then, the exfoliated WS_2 sheets were mixed with polycaprolactone (PCL)/calcium silicate (CS) to form a biocompatible WS_2-based composite. The in vivo experiments show that the bone regeneration of the WS_2-based composite was 120% superior to commercially available mineral trioxide aggregate (MTA) bone cement. Moreover, the mechanical properties of the WS_2-based composite exhibited ~300% enhancement over PCL/CS, which is one of the most commonly used bone regeneration materials. Our findings highlight the prospects for the composite of WS_2 towards the improvement of bone regeneration applications.

npj 2D Materials and Applications (2020)4:34 ; https://doi.org/10.1038/s41699-020-00168-y

INTRODUCTION

In 2020, the world's population is close to eight billion[1]. Humankind is facing two critical challenges: population ageing and global climate change[2]. Regarding the first, nearly one billion people are over 64 years of age, and bone fracture is one of the most frequent problems for all people in this demographic because of osteoporosis[3]. In response, many synthetic biocompatible materials have been developed and used in bone tissue engineering. However, most biocompatible materials are insufficient in their mechanical properties[4], lack bioactivity, have uncontrolled degradation rates[5], and thus, cannot help with native bone regeneration for certain physiological conditions[6]. Therefore, developing biocompatible materials with superior mechanical properties and osteogenic bioactivity has attracted significant attention in the field of bone tissue regeneration[7,8]. To do so, discovering functional materials is fundamental to resolving the issues mentioned above.

Transition metal dichalcogenides (TMDs) have attracted much attention over the past ten years due to their intrinsic properties[9–11]. As the most representative TMD, molybdenum disulfide (MoS_2) has been intensively studied. Although tungsten disulfide (WS_2) has a crystal structure analogous to that of MoS_2, it exhibits superior biocompatibility and physical and photoelectrochemical properties[12–14]. Lalwani et al.[15] demonstrated that WS_2 nanotubes can uniformly disperse in biodegradable polymers and are excellent reinforcing agents compared with carbon-based materials (e.g., carbon nanotubes). However, in vitro experimental results for WS_2 nanotubes are lacking. Raichman et al. used a highly electrophilic acidic Vilsmeier-Haack reagent to produce polycarboxylated functional WS_2 nanotubes that can be dispersed in polar liquids[16]. In 2018, they also found that the functionalised WS_2 is biocompatible and may come into contact with blood, indicating a high degree of biocompatibility[17]. However, there have only been a limited number of studies focussing on the preparation of WS_2 thin sheets via liquid-phase exfoliation and the application of these sheets[18–21]. There has yet to be found a simple, eco-friendly, facile method for producing WS_2 thin sheets in large quantities owing to its insolubility in common solvents, and a low degree of compatibility with common polymers[16]. In this study, the authors report on an environmentally friendly and effective strategy for scalable production of high-quality WS_2 thin sheet suspensions with the assistance of a natural pigment that exists in abundance—chlorophyll molecules. With the strategy used in this study, exfoliated WS_2 thin sheets can be produced in high concentrations. They can be thoroughly mixed with polycaprolactone (PCL) and calcium silicate (CS), which are Food and Drug Administration (FDA) approved materials, to form a WS_2/PCL/CS biocompatible composite possessing an extraordinary bone regeneration efficiency of 120%, which is superior to commercially available mineral trioxide aggregate (MTA) bone cement, and it is non-toxic for stem cells. To the best of the authors' knowledge, the current study is the first on a WS_2/PCL/CS composite to demonstrate an excellent degree of bone regeneration efficiency.

RESULTS AND DISCUSSION

Stability of WS_2 thin sheet suspension

Images of the chlorophyll-assisted exfoliated WS_2 thin sheet suspensions are shown in Fig. 1a. Figure 1b shows that no decay

[1]χ-Dimension Centre for Medical Research and Translation, China Medical University Hospital, 2 Tuh-Der Road, Taichung City 40447, Taiwan. [2]Graduate Institute of Biomedical Sciences, China Medical University, Taichung City, Taiwan. [3]School of Dentistry, China Medical University, Taichung City, Taiwan. [4]Department of Bioinformatics and Medical Engineering, Asia University, Taichung City, Taiwan. [5]Department of Applied Science, National Taitung University, 369, Sec. 2, University Road, Taitung City 95092, Taiwan. [6]Georgia Tech Manufacturing Institute, Georgia Institute of Technology, Atlanta, GA 30332, USA. [7]School of Industrial and Systems Engineering, Georgia Institute of Technology, Atlanta, GA 30332, USA. [8]School of Materials Science and Engineering, Georgia Institute of Technology, Atlanta, GA 30332, USA. ✉email: iwchen@nttu.edu.tw

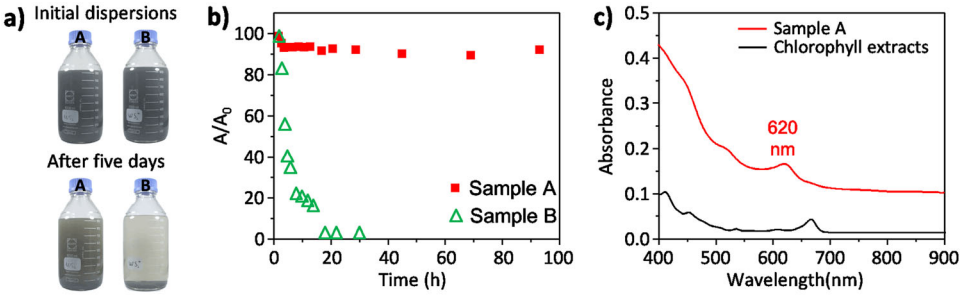

Fig. 1 Synthesis of high-quality WS2 thin sheet suspension via chlorophyll-assisted liquid-phase exfoliation. a Images of 1000 mL suspensions of bulk WS_2 in acetone with extracted chlorophyll molecules (sample A) and without extracted chlorophyll molecules (sample B); **b** Comparative stability of sample A (□) and sample B (Δ). 'A_0' represents the initial absorbance of the suspension, and 'A' depicts the measured absorbance after standing for certain periods of time; and **c** Characteristic absorbance of exfoliated WS_2 thin sheets and extracted chlorophyll molecules.

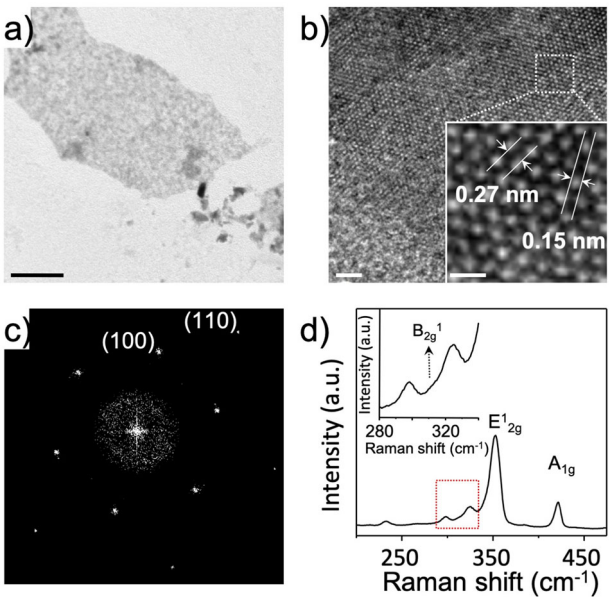

Fig. 2 Characterisation of chlorophyll-assisted exfoliated WS_2 thin sheets. a LRTEM image. Scale bar: 400 nm; **b** HRTEM image of exfoliated WS_2 monolayer (Scale bar: 2 nm) showing basal planes (100) and (110) with a repeat distance of 0.27 and 0.15 nm, respectively. The inset scale bar used is 0.5 nm. The point group of the single layer is D_{3h}[65]. **c** FFT image; and **d** Raman spectrum of exfoliated monolayer WS_2 thin sheet.

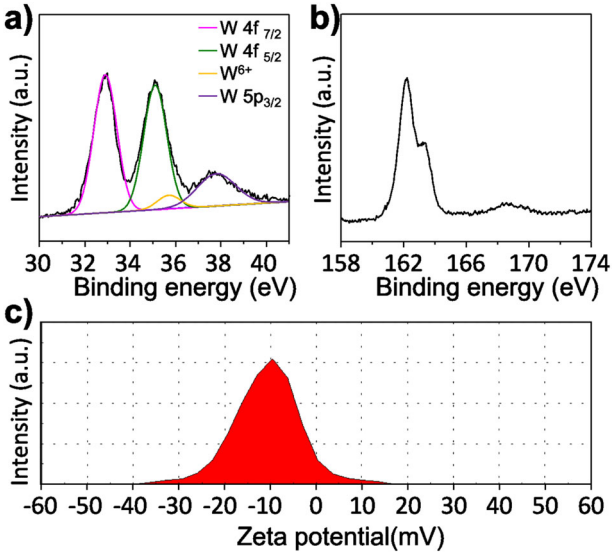

Fig. 3 XPS and zeta potential measurement of the exfoliated WS_2 thin sheets. a XPS spectra showing peak regions of W 4f and W5p; **b** S 2p core level for exfoliated WS_2 thin sheets; and **c** Zeta potential of exfoliated WS_2 thin sheets.

in the absorbance of the suspension was observed, indicating the superior stability of this study's chlorophyll-assisted liquid-phase exfoliation method in the scalable production of WS_2 thin sheets. Figure 1c shows the optical absorbance spectra of the exfoliated WS_2 thin sheet suspensions and extracted chlorophyll solution, which exhibited characteristic excitonic transitions. According to the related empirical equation[22], the layer number (*N*) of the sheets in the dispersions was close to unity. The low-resolution TEM (Fig. 2a and Supplementary Fig. 1) images show that the bulk WS_2 was exfoliated into thin sheets with the help of extracted chlorophyll molecules. Supplementary Fig. 2 shows a high-angle annular dark-field scanning transmission electron microscopy (HAADF-STEM) image, and the elemental mapping results, indicating that the W and S atoms were homogeneously distributed. The atomic percentages of W and S were 28.9% and 54.7%, respectively. In the HRTEM image with atomic resolution (Fig. 2b), the sharp edge corresponds to a monolayer single-crystal WS_2 structure. The fast Fourier transformation (FFT) in Fig. 2c and Supplementary Fig. 3 exhibit reflection spots, while the pattern of the thin sheets indicates that the crystallinity and hexagonal structure were not significantly affected by probe sonication. Figure 2d shows the unpolarised Raman spectrum measured at 532 nm of excitation. The dominant peaks at ~350 and ~420 cm^{-1} were attributed to the E^1_{2g} and A_{1g} modes, respectively. Most importantly, the $B_{2g}{}^1$ phonon (~310 cm^{-1}) peak has been reported to correspond to layer-layer interaction, which is active for multilayers but inactive for monolayers[23]. Figure 2d shows that the $B_{2g}{}^1$ phonon peak did not appear in the exfoliated high-quality WS_2 thin sheets, indicating that they are monolayer in structure[23–27]. These results validate the successful large-scale production of monolayer WS_2 thin sheets having a relatively high crystallinity.

To further examine the chemical composition of the sheets, X-ray photoelectron spectroscopy (XPS) was utilised to measure the binding energy of W and S. Figure 3a shows the core-level spectrum of W 4 f and W 5p on the sheets. Three prominent peaks appear at 32.9, 35.1, and 37.8 eV, which correspond to the W $4f_{7/2}$, W $4f_{5/2}$, and W $5p_{3/2}$ components, respectively. The peak positions correspond to a trigonal prismatic configuration of W atoms and are identical to those of the semiconducting-phase WS_2 grown

through other methods[28–30]. Meanwhile, the peak at 35.8 eV is ascribed to the characteristics of W^{6+}. The appearance of W^{6+} peaks might be on account of limited surface oxidisation of the sheets during exfoliation[30–32]. Similarly, in the core-level spectrum of S 2p, Figure 3b shows two prominent peaks at 162.2 and 163.2 eV, corresponding to the S $2p_{3/2}$ and S $2p_{1/2}$ components of WS_2, respectively. These results are superior to that of electrochemically exfoliated WS_2 sheets that oxidise the pristine charge of W^{4+} to W^{5+} and W^{6+}[33]. To gain further insight into the exfoliation mechanism, FL, FL lifetime, XPS and zeta potential measurements were conducted. The FL spectra of the extracted chlorophyll solution were measured on excitation at 610 nm, as shown by the black line in Supplementary Fig. 4a. Then, the WS_2 powder was added into the extracted chlorophyll solution without using sonication. The FL intensity of the extracted chlorophyll molecules were fully quenched as shown by the blue line in Supplementary Fig. 4a (Supplementary Video). Supplementary Fig. 4b shows the FL lifetime result of the extracted chlorophyll solution and exfoliated WS_2 thin sheets. The sheets exhibited no FL intensity, indicating that the FL property of the extracted chlorophyll molecules was quenched by the adsorbed WS_2 thin sheets. Supplementary Fig. 4c depicts the core-level spectrum of N 1s of the sheets. The binding energy locations of 399.7 and 401.6 eV represent the functional groups of the extracted chlorophyll[34–36]. The lack of a peak being located at 397.2 eV is ascribed to the absence of W-N bond formation between the sheets and the extracted chlorophyll molecules. According to the FL, FL lifetime, and N1s XPS data, the extracted chlorophyll molecules were physically adsorbed on the surface of the sheets. Moreover, the zeta potential of the sheets was −10.8 mV, as shown in Fig. 3c. The negative surface potential value is evidence of electrostatic repulsive forces between each of the sheets, resulting in a stable suspension. Xu et al.[19] utilised sub-stoichiometric amounts of lithium to exfoliate bulk WS_2 to 1–2-layer WS_2 nanosheets. However, this exfoliation process requires harsh conditions. Adilbekova et al.[37] used a less environmentally friendly alkaline solvent to exfoliate bulk WS_2 into thin sheets. However, the size of the sheets was only several tenths of a nanometre in length, which does not provide sufficient mechanical strength for bone regeneration. Coleman et al.[20] reported that the surface tension of an N-methyl-2-pyrrolido (NMP) solvent was in the range of 30–40 mJ m^{-2}, which is close to that of transition metals dichalcogenides. However, most of the WS_2 thin sheets prepared through this method were too thick. Furthermore, NMP is a highly toxic and high-temperature solvent which is not suitable for scalable production of WS_2 thin sheets. To the best of our knowledge, the current study is the first to demonstrate the scalable production of sub-micrometre sized monolayer WS_2 thin sheets with the assistance of extracted chlorophyll molecules under mild conditions.

According to density functional theory (DFT) calculations, WS_2 has the potential to be amongst the most efficient electrocatalysts because its hydrogen adsorption free energy (ΔG_{H^*}) on the WS_2 edge site is close to thermoneutral, which is similar to Pt-group metals. Liu et al.[38] demonstrated that synthesised WS_2 exhibited an onset potential of −130 mV and a Tafel slope of 80 mV dec^{-1}. Voiry et al.[18] found that Li-assisted exfoliated WS_2 thin sheets can be synthesised yielding a Tafel slope of 60 mV dec^{-1}. It is expected that the preparation of monolayer WS_2 sheets will significantly affect the catalytic performance. The electrochemical performance of the exfoliated monolayer WS_2 sheets, as the electrocatalyst on an Au electrode, were conducted using a three-electrode configuration in a 0.5 M H_2SO_4 electrolyte. Supplementary Fig. 5a shows the polarisation curves of the assembled WS_2 films with different assembly times. The onset potential and the Tafel slope of the sample labelled 'WS_2 assembly 24 h' were −118 mV (at the current density of 1 mA cm^{-2}) and 60 mV dec^{-1} (Supplementary Fig. 5b), respectively. Interestingly, unlike MoS_2, bulk WS_2 in its semiconducting form is not perceived as a good hydrogen evolution reaction (HER) electrocatalyst[18,30,38–40], but here a superior electrocatalytic performance was achieved with the chlorophyll-assisted exfoliated WS_2 thin sheets. Either a too short or a too long an assembly time led to a decrease in HER activity on the WS_2 film. A possible reason for this is that <24 h was too short a time to form a compact self-assembled film, however, increasing the incubation to 36 h resulted in the stacking of the exfoliated sheets[30]. The reduced onset potential and lower Tafel slope of the WS_2 assembled 24 h sample indicate that the free energy of the hydrogen binding to the chlorophyll-assisted exfoliated WS_2 thin sheets is closer to the thermodynamic equilibrium[30]. The Tafel slope of the 36 h-assembled films was around 95 mV dec^{-1}, which is most likely related to the higher internal resistance of the film[41,42]. In order to further understand the reason for the enhanced electrocatalytic performance, XPS analysis was carried out. Supplementary Fig. 5c shows that the WS_2 assembly 24 h sample had two sets of binding energies. The S $2p_{3/2}$ binding energy at around 162.7 eV represented the original S in WS_2, and an S $2p_{3/2}$ peak at 161.8 eV could be attributed to the S of the WS_2 assembled on the Au surface. It has been demonstrated that the electron transfer from electron-rich Au to electron-deficient S causes a decrease in binding energy for S, attesting to the presence of the S-Au bond[32,43]. Taking this into account, since the binding energy of 161.8 eV closely matches the binding energy of the S-Au bond[44], the authors believe that the peak of 161.8 eV should be attributed to the formation of the S-Au bond during the assembly process. Supplementary Fig. 5d shows a good degree of stability, where the electrocatalytic activity did not greatly change after 20 h. Therefore, the authors believe that the chlorophyll-assisted exfoliated WS_2 thin sheets have promise as a water-splitting electrocatalyst.

To enhance the HER performance of the exfoliated WS_2 thin sheets, their photoelectrochemical behaviour was further examined. Figure 4a shows the polarisation curves of the samples labelled 'WS_2 assembly 24-h-light off' and 'WS_2 assembly 24-h-light on'. Figure 4b shows that the latter sample exhibited a 277% current density increase at the potential of −50 mV. This demonstrates that the sample exhibited a superb degree of photoelectrocatalytic activity for water-splitting because the exfoliated WS_2 thin sheets can absorb visible light between 600 and 700 nm, as mentioned above. After loading limited PtNPs onto WS_2, the corresponding photocurrent showed a significant increase to 4.524 mA cm^{-2} at −50 mV under visible-light illumination (the blue dash-dot line in Fig. 4c). Surprisingly, the onset potential of the sample labelled 'WS_2 assembly 24-h-light on-with PtNPs' was further improved to −14 mV (at the current density of 1 mA cm^{-2}), as shown in Fig. 4d, which is far superior to values reported in other studies for WS_2-based materials (Supplementary Fig. 6). Here, PtNPs play two roles in the photoelectrocatalytic reaction: as an electron sink to trap photo-excited electrons from the WS_2 sheets for water reduction[45,46], and as a provider of efficient channels for electron transportation for direct water reduction[47,48].

Physical properties of WS_2/PCL/CS scaffold

The potential use of chlorophyll-assisted exfoliated WS_2 thin sheets in a wide range of applications requires the predetermination of risks they pose in living organisms[49]. Therefore, the sheets were subjected to a series of experiments to evaluate their biocompatibility and bone regeneration. To mimic bone composition, bio-ceramics of CS and PCL polymers have been widely used[50–54]. These materials are commercially available, biodegradable, biocompatible, and approved by the FDA[55]. After fully mixing these materials with exfoliated WS_2 thin sheets to form a WS_2/PCL/CS composite, a three-dimensional scaffold was successfully created by using three-dimensional printing. The

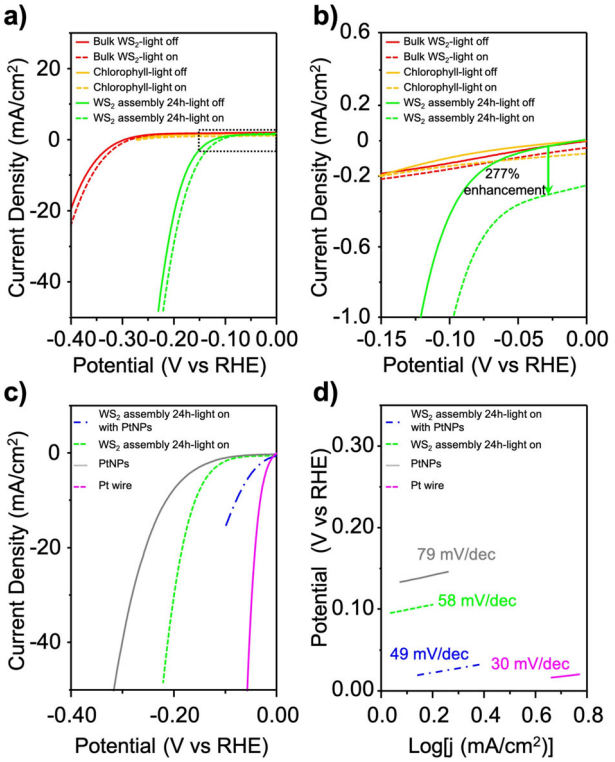

Fig. 4 Electrochemical performance of the exfoliated WS_2 thin sheets. a Polarisation curves for the bulk WS_2 (red), extracted chlorophyll molecules (orange), and WS_2 assembly 24 h (green) sample with (dashed line), and without (solid line) simulated sunlight irradiation (100 mW cm^{-2}); **b**) Magnification of dotted rectangle in (**a**); **c** Polarisation curves; and **d** Tafel slope for Pt wire, PtNPs, and assembled composites including the sample of WS_2 assembly 24-h-light on-with PtNPs and WS_2 assembly 24-h-light on.

printed scaffolds had a well-designed morphology (Fig. 5a). The interconnected macro-pore structure promotes cell in-growth and nutrient transportation, and their bioactive components can lead to osteogenesis and angiogenesis[56]. To understand the homogeneity of the chlorophyll-assisted exfoliated WS_2 thin sheets in the WS_2/PCL/CS composite, non-destructive Raman measurements were used. Figure 5b shows that the mapping spectrum of the scaffold had a uniform WS_2 signal intensity, indicating that the exfoliated WS_2 thin sheets were homogeneously distributed in the WS_2/PCL/CS composite. To further investigate the reinforcement effect of the sheets in the scaffold, compression testing was carried out. Figure 5c shows that the compression strength was enhanced from 2.0 MPa for a PCL/CS scaffold to 6.0 MPa for the WS_2/PCL/CS scaffold, a 300% improvement. The Young's modulus of the PCL/CS scaffold was 32 MPa. The Young's modulus of the composite was significantly improved to 145 MPa, which is nearly a 450% improvement. The results of the compressive modulus and strength of the scaffold reached the range of human cancellous bone tissue[57]. Such reinforcement-enhancement is related to the original properties of the exfoliated sheets[58], indicating the superior degree of dispersion of the sheets in the biocompatible matrix. In addition to understanding the biocompatibility and bioactivity of WS_2/PCL/CS scaffold, precipitated spherical mineral aggregates were observed on the surfaces of the PCL/CS and WS_2/PCL/CS scaffolds using FE-SEM. Full mineral aggregates coating both types of scaffold showed that apatite formation was not inhibited by the added WS_2 (Fig. 5d). Apatite layers are responsible for the biocompatibility and bioactivity of CS-based materials that are part of the interface of the scaffold and natural bone tissue[59].

In vitro cell behaviour effects of WS_2/PCL/CS scaffold

To evaluate the effect of cells on WS_2/PCL/CS scaffold, we used the human mesenchymal stem cells (hMSCs) to analyse Col I secretion, cell viability, alkaline phosphatase (ALP), and cell morphology. Figure 6a shows the amount of Col I adsorbed onto the scaffolds of a cell culture well (the control, abbreviated as Ctl), the PCL/CS, and the WS_2/PCL/CS. The concentration of Col I on the WS_2/PCL/CS scaffold was over two times higher than the result of Ctl, indicating the effective binding of Col I on the scaffold with the added WS_2. Col I contains several cell-binding sub-units, which in turn bind to components of cell membranes to positively influence the cell behaviour, such as adhesion and proliferation[60]. An understanding of the biocompatibility of the WS_2/PCL/CS scaffold is required, as the efficiency of cell viability is one of the critical issues affecting the results of tissue regeneration. Figure 6b shows significant enhancement of the viability of the cultured hMSCs on the WS_2/PCL/CS scaffolds, as compared to the Ctl at days 1, 3, and 7 ($p < 0.05$). This was especially true for the WS_2/PCL/CS scaffolds as a nearly 30% enhancement of the cell viability, as compared with the PCL/CS scaffolds, was observed at Day 7. This is attributed to the WS_2/PCL/CS scaffold offering better micro-environmental conditions for hMSCs viability[56]. To evaluate the osteoblastic differentiation efficiency in detail, the useful marker of ALP activity was performed. Figure 6c shows that the ALP activity for all scaffolds increased with time, and the ALP activity from hMSCs in WS_2/PCL/CS scaffolds was significantly higher than that of the Ctl and the PCL/CS scaffold at days 3, 7, and 14 ($p < 0.05$), indicating that the WS_2/PCL/CS scaffold ably supports the early steps of osteoblastic differentiation in hMSCs. Figure 6d shows that hMSCs had a better adhesion to the WS_2/PCL/CS scaffold than to the PCL/CS scaffold after 12 h. The authors believe that the WS_2/PCL/CS scaffold can adsorb more Col I on the surface so enhancing the initial cell attachment ability. Various studies have demonstrated that Col I can regulate the attachment, proliferation, and osteogenic differentiation of stem cells[56]. Overall, the cell adhesion and viability data demonstrate that the chlorophyll-assisted exfoliated WS_2 thin sheets did not exhibit any cytotoxic responses to the hMSCs. Thus, this study opens possibilities in the development of chlorophyll-assisted exfoliated WS_2 thin sheets for tissue regeneration applications.

In vivo bone regeneration efficacy of WS_2/PCL/CS scaffold

In vivo experiments were carried out (Supplementary Fig. 8) by evaluating bone regeneration in femoral defects in rabbits after the implantation of PCL/CS, WS_2/PCL/CS, and MTA scaffolds. Figure 7a shows micro-computed tomography (μCT) images of the three types of scaffolds after implantation at four and eight weeks. The implanted WS_2/PCL/CS scaffold specimen generated much more bone around the scaffold compared to the PCL/CS and MTA scaffolds. The BV/TV (Fig. 7b) and Tb.Th (Fig. 7c) values for the WS_2/PCL/CS scaffold were much higher than those of the PCL/CS and MTA scaffolds ($p < 0.05$). In comparison to MTA, the best therapeutic efficiency (scored as the extent of in vivo bone regeneration) was exhibited by the WS_2/PCL/CS scaffold. The results of the undecalcified specimens of PCL/CS, WS_2/PCL/CS, and MTA scaffolds stained by the haematoxylin and eosin (HE) stain, Von Kossa (VK) stain, and Masson's trichrome (MT) stain are shown in Fig. 7d. The HE staining showed the tissue regeneration was well formed within the defect area in the WS_2/PCL/CS scaffold, whereas tissue was minimal in the PCL/CS scaffold. The MT staining in the WS_2/PCL/CS group at eight weeks shows that the collagen area and the lumen of the blood vessels supported active osteogenesis around the scaffolds. VK staining is known to be highly visible in formed bone tissue[61]. In particular, the images of the WS_2/PCL/CS scaffold in Fig. 7d exhibit the most intense VK staining, which indicates much more extensive bone regeneration

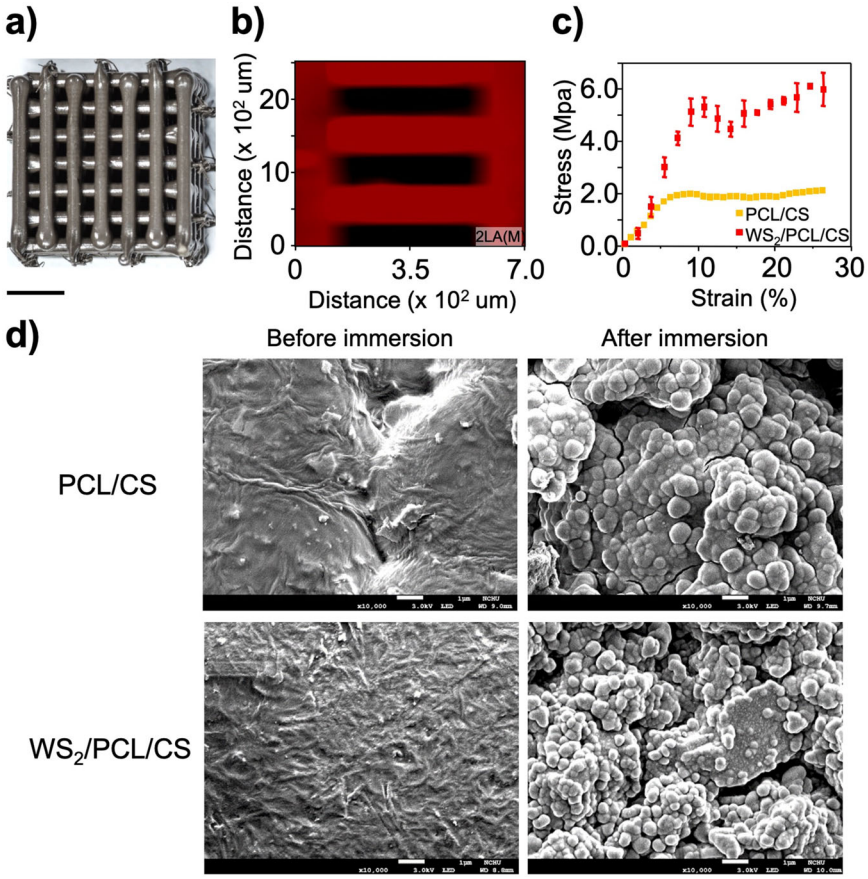

Fig. 5 Characterisation of WS_2/PCL/CS composite properties. a Photograph of WS_2/PCL/CS scaffold. The scale bar used is 2 mm; **b** Raman mapping image of WS_2/PCL/CS scaffold by extracting the frequency of the characteristic peak of WS_2 thin sheets; **c** Mechanical properties of PCL/CS and WS_2/PCL/CS scaffolds. Data presented as mean ± s.d. (s.d. standard deviation), $n = 6$ for each group; and **d** FE-SEM images of the surface microstructures of PCL/CS and WS_2/PCL/CS scaffolds, before and after being immersed in SBF.

in the WS_2/PCL/CS sample, demonstrating that the formed bone was generated around the bone defect.

In summary, this study demonstrates an eco-friendly and easy route to the scalable production of high-quality WS_2 thin sheets for bone regeneration and photoelectrochemical hydrogen generation applications. The extracted chlorophyll is a useful pigment from nature for preparing a high-concentration WS_2 thin sheet dispersion with an excellent degree of stability in a volatile solvent. The self-assembled exfoliated WS_2 thin sheets on an Au surface exhibited unusual HER photoelectrocatalytic activity with an onset potential of −14 mV and a Tafel slope of 49 mV dec^{-1}, the lowest onset potential achieved with such a low Tafel slope value that has been reported to date. According to the in vivo experiments, the bone regeneration of the WS_2/PCL/CS scaffold was 120% superior to that of commercially available MTA material. The mechanical properties of the WS_2/PCL/CS scaffold exhibited ~300% enhancement over PCL/CS, which is one of the most commonly used materials. The WS_2 added to the PCL/CS scaffold enabled the scaffold to interact with cells, resulting in excellent osteoblast adhesion and apatite deposition. The authors thus believe that these versatile WS_2 thin sheets may provide an opportunity to help resolve issues related to population ageing and global climate change.

METHODS

Chemicals

WS_2 powder (99% metals basis; ~325 mesh powder) was purchased from Alfa Aesar. PCL (PCL; MW 43,000–50,000, Polysciences, Warrington, PA), calcium oxide (CaO, Sigma-Aldrich), silica (SiO_2, High Pure Chemicals, Saitama, Japan), MTA (MTA, Sigma-Aldrich), aluminium oxide (Al_2O_3, Sigma-Aldrich), phosphate-buffered saline (PBS, Caisson, North Logan, UT), paraformaldehyde (Sigma-Aldrich), Alexa Fluor 488 dye (InvitrogenTM, ThermoFisher), 4′,6-diamidino-2-phenylindole (InvitrogenTM, ThermoFisher), and *p*-nitrophenyl phosphate (Sigma-Aldrich) were all used as received. Acetone (HPLC grade) and sulfuric acid (H_2SO_4, 99.5%, HPLC grade) were purchased from ECHO chemical Co., Ltd. All solvents were used without further purification.

Preparation of chlorophyll extracts

Green leaves (20 g) were ground in a mortar and pestle and 500 mL acetone was poured into the mortar. After standing for 8 h, the chlorophyll extracts were filtered through a 0.22 µm pore size polyvinylidene fluoride membrane to remove impurities. The filtered solution was centrifuged at 3000 rpm for 30 min and the supernatants of the chlorophyll extract solution were collected. The concentration of the chlorophyll extracts was ~5 mg L^{-1}.

Chlorophyll-assisted liquid-phase exfoliation of WS_2

WS_2 powder (5 g), 10 mL of extracted chlorophyll solution, and 240 mL acetone were added to a 500 mL glass serum bottle at a controlled temperature, and sonicated with 150 W horn sonication (Q700, QSONICA) in pulse mode for 5 h. To measure the concentration of the WS_2 suspension, 100 mL of solution was filtered through a 0.2 µm polyvinylidene fluoride membrane, and the weight of the WS_2 measured. The suspension concentration of the exfoliated WS_2 thin sheets was ~1 mg mL^{-1}.

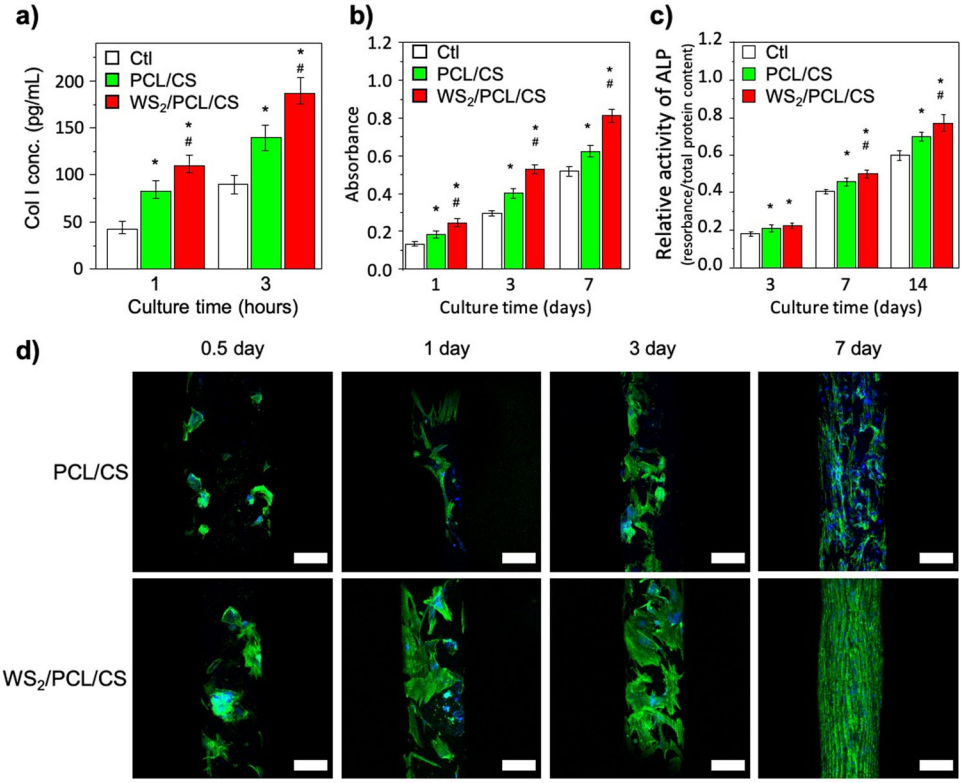

Fig. 6 In vitro cell behaviour effects of WS_2/PCL/CS scaffold. a Col I secretion; **b** Viability; and **c** ALP activity of hMSCs cultured on PCL/CS and WS_2/PCL/CS scaffolds. '*' indicates a significant difference ($p < 0.05$) compared to Ctl. '#' indicates a significant difference ($p < 0.05$) compared to the PCL/CS scaffold; **d** F-actin filaments (green) and nuclei (blue) staining of hMSCs cultured on scaffold at different time-points. Scale bar is 200 µm.

Synthesis of PtNPs

The platinum nanoparticles (PtNPs) were synthesised in glassware with a magnetic stir bar. 1 mL of 16 mM hexachloroplatinate (H_2PtCl_6), 1 mL of 40 mM tri-sodium citrate, and 38 mL of deionised water were separately added to a 200 mL two-necked bottle and stirred for a half-hour to obtain a colourless mixture. Then, 200 µL of 50 mM sodium borohydride ($NaBH_4$) was added slowly into the two-necked bottle. The colourless mixture instantaneously turned to brownish-yellow. Finally, the brownish-yellow solution was continuously stirred at room temperature for 1 h. The solution was then stored in the dark until use. All glassware used in the PtNPs synthesis experiments was thoroughly cleaned with aqua regia, rinsed with deionised water (Elga Ltd., High Wycombe, UK), and then dried in an oven before use.

Electrochemical measurements

HER experiments were measured using a CHI7279E electrochemistry workstation. Electrochemical measurements were carried out with a three-electrode configuration using 0.5 M H_2SO_4 as an electrolyte, and an Ag/AgCl electrode and a graphite electrode as the reference and counter electrodes, respectively. Linear sweep voltammetry (LSV) was performed at a rate of 1 mV s^{-1} for the polarisation curves. The I-t curve test was carried out with a controlled bias voltage.

Preparation of the calcium silicate (CS) powder

The method used for the preparation of CS powder has been described elsewhere[62]. In brief, CaO, SiO_2, and Al_2O_3 powders were used as matrix materials (composition: 70% CaO, 25% SiO_2, and 5% Al_2O_3). The oxide mixtures were sintered at 1400 °C for 2 h using a high-temperature furnace, and then the CS powder was ball-milled in ethyl alcohol using a centrifugal ball mill (S100, Retsch, Hann, Germany) for 6 h.

Fabrication of the WS_2/PCL/CS composite scaffolds

The CS matrices were produced using the thermal pressing method[63]. In a previous study[64], we demonstrated that the ratio of PCL/CS = 50/50 had better mechanical properties and cell behaviours. First, 47.5 mg PCL was placed in a 150 °C oven for 2 h. Then, 47.5 mg CS powder and 5 mg of the exfoliated WS_2 thin sheets were suspended in 5 mL alcohol and dropped into the PCL. The sample was labelled is 5% WS_2/PCL/CS. Supplementary Fig. 7 shows the cell viability of different ratios of the WS_2 scaffold. The 5% WS_2/PCL/CS composite showed a suitable condition for cell viability and hence, it was used in the study. The WS_2/PCL/CS composites were loaded into a steel syringe and heated to 100 °C in a three-dimensional printer (3DP) system (BioScaffolder 3.1, GeSiM, Grosserkmannsdorf, Germany) to produce the printable WS_2/PCL/CS composites, which were injected by applying a pressure of 500 kPa to produce a 400 µm diameter straight line. Seven lines were printed in parallel with a gap of 400 µm between the lines, forming one layer. The 3DP scaffold was plotted layer-by-layer, up to 16 layers, for bone engineering applications. The weight of the 16 layers scaffold was 0.4 g. Mechanical testing was done in accordance with ASTM D695-02a. The EZ Test machine (Shimadzu, Kyoto, Japan) was used to determine the mechanical properties of each scaffold at a loading rate of 1 mm min^{-1}. The scaffolds were printed into a 6 mm×6 mm × 10 mm rectangle. The average values and standard deviations (s.d.) of Young's modulus, and the maximum compressive strength were evaluated from the recorded stress-strain curves. Data are presented as mean ± s.d., $n = 6$ for each group.

Cell adhesion and viability

All 3DP scaffolds were soaked in 75% ethanol followed by irradiation for 1 h under UV light before the cell culture experiment. The human mesenchymal stem cells (hMSCs) were purchased from Sciencell Research Laboratories (Sciencell, Carlsbad, CA) and developed in medium (Sciencell). The cultured medium consisted of 500 mL of basal medium, 25 mL of foetal bovine serum, 5 mL of mesenchymal stem cell growth supplement and 5 mL of penicillin/streptomycin solution. The cells were seeded onto the specimens at a concentration of 5×10^4 cells per scaffold. After culturing for 1 and 3 h, the cultured medium was collected, and Col I secreted from hMSCs was analysed by an enzyme-linked immunosorbent assay kit (ELISA, Invitrogen), following the instructions in the manufacturer's manual. In addition, cell viability was determined using PrestoBlue

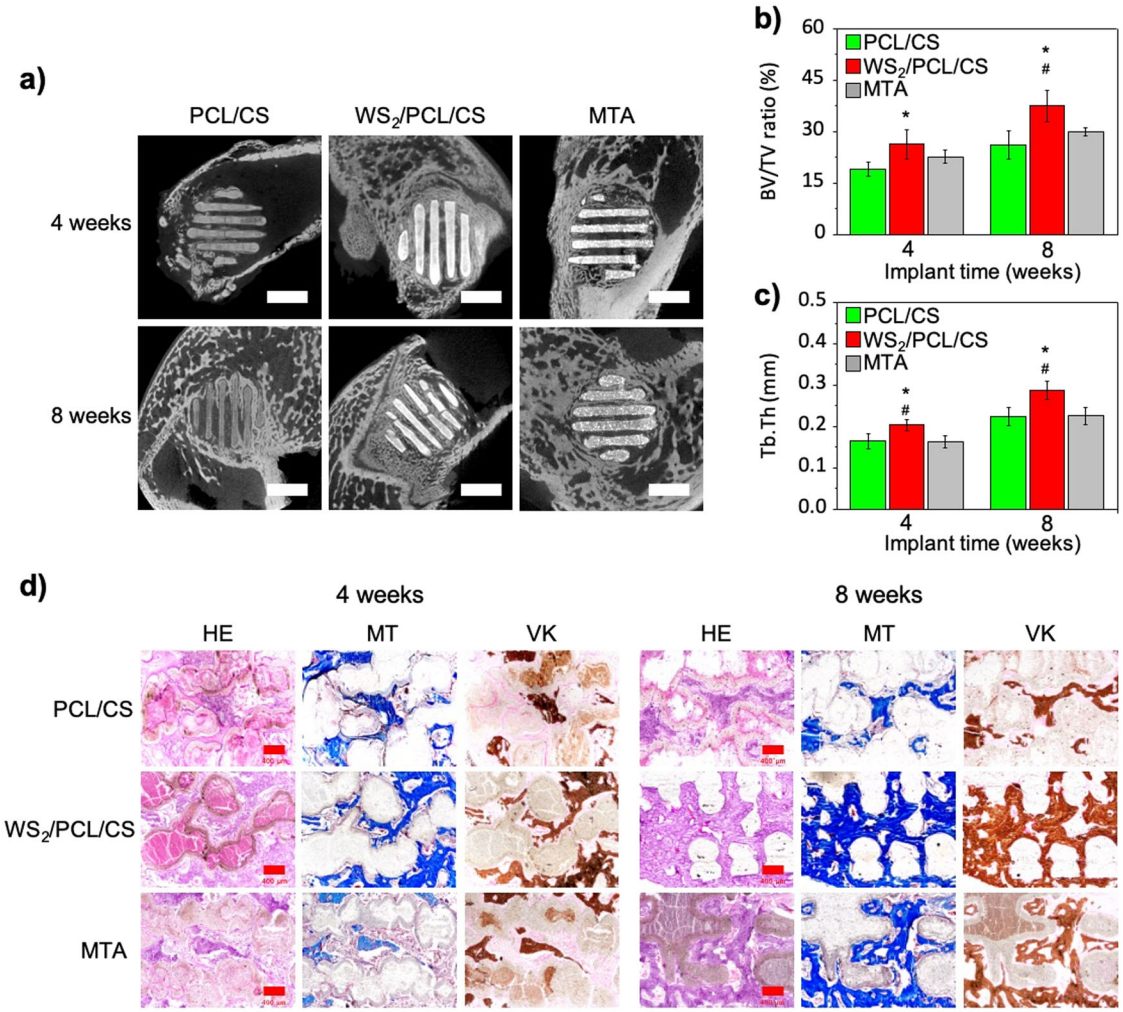

Fig. 7 In vivo bone regeneration efficacy of WS_2/PCL/CS scaffold. a Cross-sectional images of μCT; **b** Bone mass volume (BV/TV); **c** Trabecular thickness (Tb.Th) of rabbit femoral defects after four and eight weeks with PCL/CS, WS_2/PCL/CS, and MTA scaffolds. Scale bar is 3 mm. '*' indicates a significant difference ($p < 0.05$) compared to the PCL/CS scaffold. '#' indicates a significant difference ($p < 0.05$) compared to the MTA scaffold; and **d** HE staining images: haematoxylin and eosin (HE) stain (left); Masson's trichrome (MT) stain (centre); and Von Kossa (VK) stain (right) of regenerated bone mass after four and eight weeks for in vivo experiments. Scale bar is 400 μm.

assay (Invitrogen) after being directly cultured for 1, 3, and 7 days. The PrestoBlue solution (30 μL) and 300 μL DMEM were added separately to each of the 96-well plates and incubated for 30 min, after which, 100 μL was extracted from each well and placed into a fresh 96-well plate and the absorbance was measured at 570 nm with a reference wavelength of 600 nm. Cells cultured without scaffold were used as the control.

Osteogenic differentiation

After cell seeding, the osteogenic differentiation was induced using a specific osteogenic medium from StemPro™ (osteogenesis differentiation kit, Invitrogen) and ALP secretion was measured on days 3 and 7. The ALP activity of each sample was characterised using *p*-nitrophenyl phosphate as the substrate with 1 mol L^{-1} diethanolamine buffer. The reaction was terminated by adding 5 N NaOH and the absorbance recorded at 405 nm. Analysis of blank disks was used as the control.

Fluorescent staining

The cultured cells were washed with PBS, fixed in 4% paraformaldehyde for 15 min, and then permeabilised with a 0.1% Triton X-100 PBS solution at 25 °C. The F-actin filaments were labelled with phalloidin conjugated to Alexa Fluor 488 dye (Invitrogen) for 1 h. The cell nuclei were stained with 300 nM 4′,6-diamidino-2-phenylindole (DAPI) for 30 min. After washing thoroughly, the morphology was imaged using a white-light laser confocal microscope (Leica TCS SP8 X, Leica Microsystems, Heidelberg, Germany).

In vivo bone regeneration

All in vivo studies and protocols were done in accordance with relevant laws and regulations. The animal use protocol listed below has been reviewed and approved by the Institutional Animal Care and Use Committee of China Medical University, Taichung, Taiwan. The white New Zealand rabbits (2.0–2.5 kg) underwent surgery to create a standard critical-sized femoral defect. The PCL/CS, WS_2/PCL/CS, and commercially available CS-based product (MTA) scaffolds ($d = 7$ mm and $h = 8$ mm) were implanted into the defects to assess the bone regeneration capacity. Afterwards, the periosteum and related tissues were sutured, and the rabbits were kept under close examination until they recovered from the effects of the anaesthesia. They initially limped but were able to walk with a proper gait after four weeks. They had free access to food and water during the period of observation. After the four weeks, the rabbits were euthanised through CO_2 asphyxiation. The scaffolds and bone specimens of the rabbits were then harvested and subsequently fixed using 10% formalin. Images of all in vivo specimens were taken with a high 360° spatial resolution micro-CT camera (μ-CT, SkyScan 1076, Skyscan Inc., Kontich, Belgium). The SkyScan software was used to recognise bone tissue and analyse the bone volume per tissue volume (BV/TV) and trabecular thickness (Tb.Th) in the 3D model. The specimens were then embedded in OCT (KMA-0100-00A, CellPath Ltd., Newtown, Wales, UK), without being decalcified, and sectioned (6 μm). The sections were stained with a haematoxylin and eosin stain kit, a modified Masson's Trichrome stain kit

(ScyTek Lab., West Logan, UT, USA), and a Von Kossa kit (ScyTek) in accordance with the manufacturers' instructions.

Characterisation

The exfoliated 2D material thin sheets were deposited onto a silicon substrate for Raman and attenuated total reflectance Fourier-transform infrared spectroscopy (ATR-FTIR) studies. Raman spectra were recorded using an iHR550 spectrometer (Horiba Jobin Yvon) with a 532 nm laser source in ambient conditions, a laser power of <100 mW, a laser spot-size of 5 µm, and the signal of silicon at 520.7 cm^{-1} as a reference. ATR-FTIR data were recorded with a Perkin-Elmer Frontier infrared spectrometer equipped with a deuterated-triglycine sulfate detector. The UV-vis spectra were recorded on a Unicam UV-300 UV-vis spectrophotometer. The fluorescence (FL) spectra were measured using an FL spectrophotometer (Hitachi F-7000, Japan) at room temperature. A multi-well plate reader (TECAN Infinite Pro M200; Tecan, Männedorf, Switzerland) was used for molecular biology analysis. The compressive strength of the 3DP scaffolds was tested on an EZ-Test machine (Shimadzu, Kyoto, Japan) under a loading rate of 1 mm min^{-1}. The images of the exfoliated WS_2 thin sheets were obtained using a low-resolution transmission electron microscope (LRTEM; JEOL JEM-2100) and a high-resolution transmission electron microscope (HRTEM; Hitachi H-7100, JEM-ARM200F and JEM-ARM200FTH). The morphology of the composite paper was imaged by a field emission scanning electron microscope (FE-SEM; JEOL JSM-7600F).

Statistical analysis

A one-way analysis of the variant statistical data was used to evaluate the significance of the differences between the means in the measured data. A Scheffe's multiple comparison test was used to determine the significance of the deviations in the data for each specimen. In all cases, the results were considered to be statistically significant with a p-value < 0.05.

Reporting summary

Further information on experimental design is available in the Nature Research Reporting Summary linked to this paper.

DATA AVAILABILITY

The data from this work are available upon reasonable request from the corresponding author I.-W.P. Chen.

Received: 11 March 2020; Accepted: 15 September 2020;
Published online: 13 October 2020

REFERENCES

1. *U.S. and World Population Clock*, https://www.census.gov/popclock/ (2020).
2. Cohen, J. E. Population and climate change. *Proc. Am. Philos. Soc.* **154**, 158–182 (2010).
3. Sözen, T., Özışık, L. & Başaran, N. Ç. An overview and management of osteoporosis. *Eur. J. Rheumatol.* **4**, 46–56 (2017).
4. Ghorai, S. K., Maji, S., Subramanian, B., Maiti, T. K. & Chattopadhyay, S. Coining attributes of ultra-low concentration graphene oxide and spermine: an approach for high strength, anti-microbial and osteoconductive nanohybrid scaffold for bone tissue regeneration. *Carbon* **141**, 370–389 (2019).
5. Guelcher, S. A. et al. Synthesis, mechanical properties, biocompatibility, and biodegradation of polyurethane networks from lysine polyisocyanates. *Biomaterials* **29**, 1762–1775 (2008).
6. Gupta, K. K. et al. Polycaprolactone composites with TiO_2 for potential nanobiomaterials: tunable properties using different phases. *Phys. Chem. Chem. Phys.* **14**, 12844–12853 (2012).
7. Fong, E. L. S., Watson, B. M., Kasper, F. K. & Mikos, A. G. Building bridges: leveraging interdisciplinary collaborations in the development of biomaterials to meet clinical needs. *Adv. Mater.* **24**, 4995–5013 (2012).
8. Puppi, D., Chiellini, F., Piras, A. M. & Chiellini, E. Polymeric materials for bone and cartilage repair. *Prog. Polym. Sci.* **35**, 403–440 (2010).
9. Manzeli, S., Ovchinnikov, D., Pasquier, D., Yazyev, O. V. & Kis, A. 2D transition metal dichalcogenides. *Nat. Rev. Mater.* **2**, 17033 (2017).
10. Nicolosi, V., Chhowalla, M., Kanatzidis, M. G., Strano, M. S. & Coleman, J. N. Liquid exfoliation of layered materials. *Science* **340**, 1226419 (2013).
11. Rao, C. N. R., Matte, H. S. S. R. & Maitra, U. Graphene analogues of inorganic layered materials. *Angew. Chem. Int. Ed.* **52**, 13162–13185 (2013).
12. Jamison, W. E. & Cosgrove, S. L. Friction characteristics of transition-metal disulfides and diselenides. *ASLE Trans.* **14**, 62–72 (1971).
13. Sobczynski, A. et al. Tungsten disulfide: a novel hydrogen evolution catalyst for water decomposition. *J. Phys. Chem.* **92**, 2311–2315 (1988).
14. Teo, W. Z., Chng, E. L. K., Sofer, Z. & Pumera, M. Cytotoxicity of exfoliated transition-metal dichalcogenides (MoS_2, WS_2, and WSe_2) is lower than that of graphene and its analogues. *Chem. Eur. J.* **20**, 9627–9632 (2014).
15. Lalwani, G. et al. Tungsten disulfide nanotubes reinforced biodegradable polymers for bone tissue engineering. *Acta Biomater.* **9**, 8365–8373 (2013).
16. Raichman, D., Strawser, D. A. & Lellouche, J.-P. Covalent functionalization/polycarboxylation of tungsten disulfide inorganic nanotubes (INTs-WS_2). *Nano Res.* **8**, 1454–1463 (2015).
17. Laloy, J. et al. Impact of functional inorganic nanotubes f-INTs-WS_2 on hemolysis, platelet function and coagulation. *Nano Converg.* **5**, 31 (2018).
18. Voiry, D. et al. Enhanced catalytic activity in strained chemically exfoliated WS_2 nanosheets for hydrogen evolution. *Nat. Mater.* **12**, 850–855 (2013).
19. Xu, D. et al. High yield exfoliation of WS_2 crystals into 1-2 layer semiconducting nanosheets and efficient photocatalytic hydrogen evolution from WS_2/CdS nanorod composites. *ACS Appl. Mater. Interfaces* **10**, 2810–2818 (2018).
20. Coleman, J. N. et al. Two-dimensional nanosheets produced by liquid exfoliation of layered materials. *Science* **331**, 568–571 (2011).
21. Bhandavat, R., David, L. & Singh, G. Synthesis of surface-functionalized WS_2 nanosheets and performance as Li-ion battery anodes. *J. Phys. Chem. Lett.* **3**, 1523–1530 (2012).
22. Backes, C. et al. Production of highly monolayer enriched dispersions of liquid-exfoliated nanosheets by liquid cascade centrifugation. *ACS Nano* **10**, 1589–1601 (2016).
23. Zhao, W. et al. Lattice dynamics in mono- and few-layer sheets of WS_2 and WSe_2. *Nanoscale* **5**, 9677–9683 (2013).
24. Lin, Y.-C. et al. Stable 1T tungsten disulfide monolayer and its junctions: growth and atomic structures. *ACS Nano* **12**, 12080–12088 (2018).
25. Li, J. et al. A typical defect-mediated photoluminescence and resonance Raman spectroscopy of monolayer WS_2. *J. Phys. Chem. C* **123**, 3900–3907 (2019).
26. Peimyoo, N. et al. Thermal conductivity determination of suspended mono- and bilayer WS_2 by Raman spectroscopy. *Nano Res.* **8**, 1210–1221 (2015).
27. Yue, Y. et al. Two-Dimensional High-Quality Monolayered Triangular WS_2 Flakes for Field-Effect Transistors. *ACS Appl. Mater. Interfaces* **10**, 22435–22444 (2018).
28. Zhang, J. et al. Electrochemical detection of adenine and guanine using a three-dimensional WS_2 nanosheet/graphite microfiber hybrid electrode. *Electrochem. Commun.* **99**, 75–80 (2019).
29. Mahler, B., Hoepfner, V., Liao, K. & Ozin, G. A. Colloidal synthesis of 1T-WS_2 and 2H-WS_2 nanosheets: applications for photocatalytic hydrogen evolution. *J. Am. Chem. Soc.* **136**, 14121–14127 (2014).
30. Lukowski, M. A. et al. Highly active hydrogen evolution catalysis from metallic WS_2 nanosheets. *Energy Environ. Sci.* **7**, 2608–2613 (2014).
31. Liu, S. et al. Binder-free WS_2 nanosheets with enhanced crystallinity as stable negative electrode for flexible asymmetric supercapacitors. *J. Mater. Chem. A* **5**, 21460–21466 (2017).
32. Sarma, P. V., Tiwary, C. S., Radhakrishnan, S., Ajayan, P. M. & Shaijumon, M. M. Oxygen incorporated WS_2 nanoclusters with superior electrocatalytic properties for hydrogen evolution reaction. *Nanoscale* **10**, 9516–9524 (2018).
33. Leong, S. X. et al. 2H→1T phase change in direct synthesis of WS_2 nanosheets via solution-based electrochemical exfoliation and their catalytic properties. *ACS Appl. Mater. Interfaces* **9**, 26350–26356 (2017).
34. Barazzouk, S., Bekalé, L. & Hotchandani, S. Enhanced photostability of chlorophyll-a using gold nanoparticles as an efficient photoprotector. *J. Mater. Chem.* **22**, 25316 (2012).
35. Rocks, C., Maguire, P., Svrcek, V. & Mariotti, D. Understanding surface chemistry during $MAPbI_3$ spray deposition and its effect on photovoltaic performance. *J. Mater. Chem. C* **5**, 902–916 (2017).
36. Yu, B. et al. Functionalized graphene oxide/phosphoramide oligomer hybrids flame retardant prepared via in situ polymerization for improving the fire safety of polypropylene. *RSC Adv.* **4**, 31782–31794 (2014).
37. Adilbekova, B. et al. Liquid phase exfoliation of MoS_2 and WS_2 in aqueous ammonia and their application in highly efficient organic solar cells. *J. Mater. Chem. C* **8**, 5259 (2020).
38. Liu, W. et al. The effects of exfoliation, organic solvents and anodic activation on the catalytic hydrogen evolution reaction of tungsten disulfide. *Nanoscale* **9**, 13515–13526 (2017).
39. Lin, J. et al. Enhanced electrocatalysis for hydrogen evolution reactions from WS_2 nanoribbons. *Adv. Energy Mater.* **4**, 1301875 (2014).

40. Shifa, T. A. et al. A vertical-oriented WS_2 nanosheet sensitized by graphene: an advanced electrocatalyst for hydrogen evolution reaction. *Nanoscale* **5**, 14760–14765 (2015).
41. Laursen, A. B., Kegnæs, S., Dahl, S. & Chorkendorff, I. Molybdenum sulfides-efficient and viable materials for electro- and photoelectrocatalytic hydrogen evolution. *Energy Environ. Sci.* **5**, 5577–5591 (2012).
42. Wang, T. et al. Enhanced electrocatalytic activity for hydrogen evolution reaction from self-assembled monodispersed molybdenum sulfides nanoparticles on an Au electrode. *Energy Environ. Sci.* **6**, 625–633 (2013).
43. Kristensen, J., Zhang, J., Chorkendorff, I., Ulstrup, J. & Ooi, B. L. Assembled monolayers of Mo_3S^{4+} clusters on well-defined surfaces. *Dalton Trans* **33**, 3985–3990 (2006).
44. Bourg, M.-C., Badia, A. & Lennox, R. B. Gold sulfur bonding in 2D and 3D self-assembled monolayers: XPS characterization. *J. Phys. Chem. B* **104**, 6562–6567 (2000).
45. Cao, S.-W. et al. Preparation of Au-$BiVO_4$ heterogeneous nanostructures as highly efficient visible-light photocatalysts. *ACS Appl. Mater. Interfaces* **4**, 418–423 (2011).
46. Yang, Y. Z., Chang, C.-H. & Idriss, H. Photo-catalytic production of hydrogen form ethanol over M/TiO_2 catalysts (M = Pd, Pt or Rh). *Appl. Catal. B: Environ.* **67**, 217–222 (2006).
47. Chen, I.-W. P. et al. Scalable synthesis of two-dimensional nano-sheet materials with chlorophyll extracts: enhancing the hydrogen evolution reaction. *Green. Chem.* **20**, 525–533 (2018).
48. Ko, C.-H., Huang, M.-J., Fu, M.-D. & Chen, C.-H. Superior contact for single-molecule conductance: electronic coupling of thiolate and isothiocyanate on Pt, Pd, and Au. *J. Am. Chem. Soc.* **132**, 756–764 (2010).
49. Lu, J. et al. Multilayered graphene hydrogel membranes for guided bone regeneration. *Adv. Mater.* **28**, 4025–4031 (2016).
50. Nieto, A. et al. Three dimensional graphene foam/polymer hybrid as a high strength biocompatible scaffold. *Adv. Funct. Mater.* **25**, 3916–3924 (2015).
51. Qiu, K. et al. Electrophoretic deposition of dexamethasone-loaded mesoporous silica nanoparticles onto poly(L-lactic acid)/poly(ε-caprolactone) composite scaffold for bone tissue engineering. *ACS Appl. Mater. Interfaces* **8**, 4137–4148 (2016).
52. Shie, M.-Y., Chiang, W.-H., Chen, I.-W. P., Liu, W.-Y. & Chen, Y.-W. Synergistic acceleration in the osteogenic and angiogenic differentiation of human mesenchymal stem cells by calcium silicate-graphene composites. *Mater. Sci. Eng. C: Mater. Biol. Appl.* **73**, 726–735 (2017).
53. Wei, J. et al. Preparation and characterization of bioactive calcium silicate and poly(ε−caprolactone) nanocomposite for bone tissue regeneration. *J. Biomed. Mater. Res. A* **90**, 702–712 (2009).
54. Wang, W. et al. Enhancing the hydrophilicity and cell attachment of 3D Printed PCL/graphene scaffolds for bone tissue engineering. *Materials* **9**, 992 (2016).
55. Middleton, J. C. & Tipton, A. J. Synthetic biodegradable polymers as orthopedic devices. *Biomaterials* **21**, 2335–2346 (2000).
56. Kajave, N. S., Schmitt, T., Nguyen, T.-U. & Kishore, V. Dual crosslinking strategy to generate mechanically viable cell-laden printable constructs using methacrylated collagen bioinks. *Mater. Sci. Eng. C: Mater. Biol. Appl.* **107**, 110290 (2020).
57. Henkel, J. et al. Bone regeneration based on tissue engineering conceptions. *Bone Res.* **1**, 216–248 (2013).
58. Leffler, P. E. & Kazantzis, G. *Handbook on the Toxicology of Metals 4E*. Vol. 2 1297–1306 (2015).
59. Liu, X., Ding, C. & Chu, P. K. Mechanism of apatite formation on Wollastonite coatings in simulated body fluids. *Biomaterials* **25**, 1755–1761 (2004).
60. Shie, M.-Y. & Din, S.-J. Integrin binding and MAPK signal pathways in primary cell responses to surface chemistry of calcium silicate cements. *Biomaterials* **34**, 6589–6606 (2013).
61. Wu, Y.-H. A. et al. 3D-printed bioactive calcium silicate/poly-ε-caprolactone bioscaffolds modified with biomimetic extracellular matrices for bone regeneration. *Int. J. Mol. Sci.* **20**, 942 (2019).
62. Chen, Y.-W., Yeh, C.-H. & Shie, M.-Y. Stimulatory effects of the fast setting and suitable degrading Ca-Si-Mg cement on both cementogenesis and angiogenesis differentiation of human periodontal ligament cells. *J. Mater. Chem. B* **3**, 7099–7108 (2015).
63. Chiu, Y.-C., Fang, H.-Y., Hsu, T.-T., Lin, C.-Y. & Shie, M.-Y. The characteristics of mineral trioxide aggregate/polycaprolactone 3-dimensional scaffold with osteogenesis properties for tissue regeneration. *J. Endod.* **43**, 923–929 (2017).
64. Lin, Y.-H. et al. The synergistic effects of graphene-contained 3D-printed calcium silicate/poly-ε-caprolactone scaffolds promote FGFR-induced osteogenic/angiogenic differentiation of mesenchymal stem cells. *Mater. Sci. Eng. C: Mater. Biol. Appl.* **104**, 109887 (2019).
65. Wirtz, A. M.-S. L. Phonons in single and few-layer MoS_2 and WS_2. *Phys. Rev. B* **84**, 155413 (2011).

ACKNOWLEDGEMENTS

This research is supported by the Ministry of Science and Technology, Taiwan (MOST 107-2628-M-143-001-MY2; 109-2811-M-143-500; 109-2628-M-143-001-MY3; 109-2218-E-039-001) and China Medical University, Taiwan (CMU109-MF-01). We gratefully thank Ms. Chia-Ying Chien, Su-Jen Ji, and Yin-Mei Chang of the Ministry of Science and Technology (National Taiwan University and National Tsing-Hua University) for their assistance in the electron microscopy experiments.

AUTHOR CONTRIBUTIONS

I.-W.P.C. designed this work. I.-W.P.C., C.-H. H., Y.-C. L. and M.-Y.S. prepared the materials and characterised them. I.-W.P.C. analysed the material characterisation and Raman spectroscopy data. M.-Y.S., Y.-W.C. and B. W. analysed the mechanical testing and bone regeneration data and prepared the relevant part of the manuscript. All authors discussed the experimental results and commented on the paper. I.-W.P.C. wrote the manuscript.

COMPETING INTERESTS

The authors declare no competing interests. All in vivo studies and protocols were done in accordance with relevant rules and regulations. The animal use protocol listed below has been reviewed and approved by the Institutional Animal Care and Use Committee of China Medical University, Taichung, Taiwan.

ADDITIONAL INFORMATION

Supplementary information is available for this paper at https://doi.org/10.1038/s41699-020-00168-y.

Correspondence and requests for materials should be addressed to I.-W.P.C.

Reprints and permission information is available at http://www.nature.com/reprints

Publisher's note Springer Nature remains neutral with regard to jurisdictional claims in published maps and institutional affiliations.